Inorganica Chimica Acta 589 (2026) 122904

Contents lists available at ScienceDirect

Inorganica Chimica Acta

journal homepage: www.elsevier.com/locate/ica

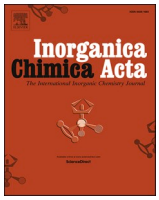

Silane-modified lanthanide complexes for integration into hybrid coatings and nanoparticles: thermal sensing applications and live cell labeling

Ivan Sedmak [a], Aljoša Bolje [b], Jakob Kljun [c], Rok Podlipec [d], Hana Kokot [d], Sebastjan Nemec [d,1], Slavko Kralj [b,d], Peter Rodič [d], Iztok Golobič [a], Stane Pajk [b,*]

[a] University of Ljubljana, Faculty of Mechanical Engineering, Aškerčeva cesta 6, 1000 Ljubljana, Slovenia
[b] University of Ljubljana, Faculty of Pharmacy, Aškerčeva cesta 7, 1000 Ljubljana, Slovenia
[c] University of Ljubljana, Faculty of Chemistry and Chemical Technology, Večna pot 113, 1000 Ljubljana, Slovenia
[d] Jožef Stefan Institute, Jamova cesta 39, 1000 Ljubljana, Slovenia

ARTICLE INFO

Keywords:
Eu complex
Silica nanoparticles
PMMA-siloxane silica coating
Thermometry
Photostability

ABSTRACT

Temperature sensing at the micro- and nanoscale remains a significant challenge due to the limitations of conventional techniques in spatial resolution and invasiveness. Here, we report the development of luminescent, temperature-sensitive coatings and nanoparticles based on a newly synthesized europium (Eu) complex integrated into a composite poly(methyl methacrylate)-siloxane-silica (PMMA-siloxane silica) matrix. The Eu complex, identified as the most promising candidate among three lanthanide complexes, was functionalized with silyl ethers via copper-catalyzed azide-alkyne cycloaddition and successfully incorporated into thin PMMA-siloxane silica films on glass surfaces and within silica nanoparticles. These materials exhibited strong thermal responsiveness, chemical stability, and suitability for high-resolution temperature sensing. Furthermore, Eu-loaded silica nanoparticles showed a distinct fluorescent signal and multiplexing capability in live-cell confocal microscopy and were internalized by lung epithelial cells (LA-4 cell line), highlighting their potential as bioimaging probes for localized intracellular temperature sensing. Although some photobleaching was observed under prolonged excitation, the materials demonstrated sufficient chemical and mechanical stability, making them promising for luminescent temperature sensing and live-cell imaging. These results establish the developed Eu-based hybrid materials as robust, non-invasive luminescent probes for high-resolution thermal sensing and cellular imaging.

1. Introduction

Today, temperature measurements represent a significant segment of the sensor market, underlining its indispensable role in a wide range of applications in different sectors. There are many methods of measuring temperature, but they often require invasive probes in direct contact with the material being measured. Thermocouples and thermistors currently form the basis of most temperature measurement techniques. However, these conventional techniques have their limitations, particularly in terms of spatial resolution in the micro and nano range, making them unsuitable for measurements below 10 μm. At this small scale, they interfere with the monitored system and require electrical connections and couplings with peripheral instrumentation [1,2]. Conversely, non-invasive techniques such as IR thermometry, thermoreflectance, Raman thermometry, and liquid crystal thermography offer the advantage of high spatial resolution and accurate thermal measurements, but their inherent limitations often hinder their reliability for precise quantitative analysis[3].

Luminescence thermometry has evolved into a technology that enables non-invasive temperature measurements and offers high spatial resolution (<10 μm), considerable relative thermal sensitivity (>1 % K^{-1}) and fast acquisition times (<1 ms). The method is based on the temperature-dependent properties of phosphor emission, such as changes in emission intensity, shifts in emission wavelength or changes in emission lifetime [1,4–6]. Various phosphor materials are used in luminescence thermometry, including organic dyes [7], green fluorescent proteins [8], fluorescent polymers [9], lanthanide-based materials [10–12], quantum dots [13] and nanodiamonds [14], to name a few. In

* Corresponding author.
E-mail address: stane.pajk@ffa.uni-lj.si (S. Pajk).
[1] Current address: University of Nova Gorica, Materials Research Laboratory, Vipavska cesta 11c, 5270 Ajdovščina, Slovenia (S.N.)

https://doi.org/10.1016/j.ica.2025.122904
Received 25 August 2025; Received in revised form 5 September 2025; Accepted 5 September 2025
Available online 8 September 2025

particular, lanthanide-based materials, which are characterized by electron transitions within the 4f orbitals, produce temperature-dependent emission spectra consisting of narrow bands corresponding to these transitions [15,16]. These materials have been used to measure temperatures over a wide range, from cryogenic to physiological conditions, and for intracellular thermometry, respectively [1,17]. In addition, the intensity ratio between two emission bands can be used to determine absolute temperatures at thermal equilibrium [4]. Lanthanides for thermometry are usually incorporated into various host materials, including molecular complexes, organic-inorganic hybrids and a variety of nanomaterials [1]. In the case of molecular complexes, lanthanides form complexes with organic ligands such as 1,3-diketones [18,19]. Since the emission of isolated lanthanide ions is typically weak, mainly due to their low molar excitation coefficients, organic ligands act as light-absorbing antennas, facilitating energy transfer to the central lanthanide ion [15,20]. While organic ligands are susceptible to photodegradation, their incorporation into materials generally improves their photostability and overall chemical stability [15].

Extending their utility beyond basic temperature sensing, lanthanide-based materials have garnered significant interest as fluorescent probes and sensors in bioanalytical applications [21,22]. Their unique photophysical properties, including an exceptionally large Stokes shift and sharp emission bands, make them highly advantageous for multiplexed imaging, based on luminescence resonance energy transfer (LRET), where multiple fluorescent probes can be distinguished based on their emission characteristics [21]. Another key advantage of lanthanide-based probes is their long fluorescence lifetimes, which can be effectively exploited in imaging and analytical assays using time-gated detection [23,24]. In fluorescence imaging, autofluorescence from biological samples often reduces contrast and sensitivity, particularly when using organic fluorophores with short-lived emissions. However, lanthanide-based probes circumvent this issue by allowing fluorescence measurement to occur after a controlled delay following excitation, selectively capturing their long-lived emission while suppressing short-lived background signals. This principle is similarly applied in time-resolved fluorescence assays, which are widely used in bioanalytical applications such as immunoassays, nucleic acid detection, and biosensing [21].

In this study, we developed a temperature-sensitive organic-inorganic hybrid thin coating by incorporating an europium complex into a PMMA-siloxane silica matrix [25–29], and a temperature sensitive lanthanide-loaded silica nanoparticles for multi-environment thermal sensing. Our previous research on Er/Yb co-doped transparent glass-ceramics for thermal sensing highlighted challenges related to structural fragility and limited applicability to non-planar surfaces [3,30,31]. To address these limitations, we designed a thermosensitive coating capable of conforming to irregular surfaces while enabling high-resolution thermal imaging. This was achieved through the synthesis of three novel alkyne-functionalized lanthanide complexes, among which the europium complex exhibited the most promising thermal response. Functionalization with silyl ethers via copper-catalyzed azide-alkyne cycloaddition (CuAAC) reaction enabled its successful integration into the PMMA-siloxane silica matrix as a thin film on glass surfaces or within silica nanoparticles. The resulting material demonstrated strong chemical and physical robustness, providing a stable platform for temperature sensing. While fluorescence microscopy studies indicated some degree of photobleaching, particularly in Eu-loaded coatings, this effect was not detrimental to the overall performance and remained manageable under optimized experimental conditions. Importantly, the internalisation of Eu-loaded nanoparticles by live lung epithelial cells (LA-4 cell line) highlights their potential as bioimaging probes, paving the way for broader applications in cellular imaging. These findings underscore the potential of our europium-based materials for use in both thermal sensing and bioanalytical applications, with future optimization focusing on enhancing photostability to extend their usability in long-term imaging and sensing environments.

2. Experimental

2.1. Materials and methods

All reagents were purchased from commercial vendors (Merck-Sigma Aldrich, TCI, Acros Organics, Abcr, Janssen, Fluka, STREM, Alfa Aesar) and were used as supplied. The PMMA-siloxane silica solution and lanthanide-loaded silica nanoparticles were prepared from methyl methacrylate (MMA, 99.0 % Sigma-Aldrich, Germany), 3-methacryloxypropyl trimethoxysilane (MAPTMS, ≥ 98 % Sigma-Aldrich, USA) and tetraethyl orthosilicate (TEOS, 99.9 %, Sigma-Aldrich, Germany). Dimethylsulfoxide (DMSO) was purchased from Merck Kga (Darmstadt, Germany). Other used solvents/chemicals for PMMA-siloxane silica were tetrahydrofuran (THF: anhydrous, ≥99.9 %, inhibitor-free, Sigma-Aldrich, Germany), ethanol (EtOH: absolute, ≥99.8 %, Sigma-Aldrich, Germany), benzoyl peroxide (BPO, Aldrich, Germany), nitric acid (HNO_3, > 70 %, Sigma-Aldrich, Italy) and deionized water. Deionized water was prepared in the laboratory on an Adrona A30 water purifying system (Adrona, Riga, Latvia). An alkoxysilane for binding with lanthanide complexes was (3-azidopropyl)triethoxysilane provided by Gelest (USA). Dry THF was distilled from a benzophenone-ketyl/sodium still and kept over 4 Å molecular sieves under argon. For TLC, Merck silica plates (60 F254, 0.25 mm) were used, and spots were detected under UV light (254 or 365 nm) or visualized by ninhydrin or phosphomolybdate staining. ^{1}H and ^{13}C NMR spectra were recorded at the University of Ljubljana, Faculty of Pharmacy with a Bruker AVANCE III 400, using acetone-d_6, methanol-d_4 or DMSO-d_6 as solvents. All chemical shifts are reported in ppm, with ^{1}H and ^{13}C resonances referenced to the residual solvent signal as internal standard. The following abbreviations are used to describe signal multiplicities: s – singlet, bs – broad singlet, app s – apparent singlet, d – doublet, dd – doublet of doublets, t – triplet, q – quartet, m – multiplet, br = broad. Coupling constants (J) are given in Hertz (Hz). NMR spectra of selected compounds are available in the Supporting Information (Fig. S1–10). High-resolution mass measurements (HRMS) were performed on a Thermo Scientific Q Exactive Plus mass spectrometer.

2.2. Synthesis of ligands

2.2.1. 4,4,4-Trifluoro-1-(4-(prop-2-yn-1-yloxy)phenyl)butane-1,3-dione (LH^1)

Acetophenone **1** [32] (7,75 g; 44, 5 mmol; 1 equiv) was dissolved in THF (70 mL) and cooled down on an ice bath. NaH (60 % dispersion in paraffin; 7,12 g; 178 mmol; 4 equiv) was added portion wise, followed by ethyl 2,2,2-trifluoroacetate (21,18 mL; 178 mmol; 4 equiv). The reaction mixture was left to reach room temperature and mix overnight. To quench the reaction, a saturated solution of NH_4Cl (5 mL) was then added dropwise. Solvents were removed under reduced pressure and the residue was dissolved in EtOAc (100 mL). Resulted solution was transferred to the separatory funnel and washed with 2 M HCl (2 × 30 mL), water (30 mL), saturated solution of $NaHCO_3$ (30 mL) and brine (30 mL). Organic phase was dried over Na_2SO_4 and the solvents were removed under reduced pressure. Crude product was purified by flash chromatography, (EtOAc:hexane, 1:4), to give the desired product (61 %) as a light red solid. ^{1}H NMR (400 MHz, $CDCl_3$) δ 15.36 (bs, 1H), 8.00–7.89 (m, 2H), 7.12–7.01 (m, 2H), 6.51 (s, 1H), 4.78 (d, J = 2.4 Hz, 2H), 2.58 (t, J = 2.4 Hz, 1H). ^{13}C NMR (101 MHz, $CDCl_3$) δ 186.09, 176.12 (q, J = 36.4 Hz), 162.44, 130.07, 126.30, 117.48 (q, J = 282.9 Hz), 115.37, 91.81, 91.79, 77.54, 76.60, 56.10. HRMS (ESI): m/z calcd for $C_{13}H_8O_3F_3$ $[M\text{-}H]^-$ 269.04310; found 269.04335.

2.2.2. 4-(5-Hydroxy-3-(trifluoromethyl)-1H-pyrazol-1-yl)benzoic acid (2)

Ethyl 4,4,4-trifluoroacetoacetate (4.06 mL, 27.75 mmol, 1 equivalent) and 4-hydrazineylbenzoic acid (4.22 g, 27.75 mmol, 1 equivalent) were dissolved in AcOH (10 mL) and mixed at 140 °C overnight. The reaction was cooled down, 5 mL of water was added and the mixture was

stirred for 1 h. The precipitate was filtered off and dried to give the desired product (66 %) as a light grey solid. **^{1}H NMR** (400 MHz, DMSO-d_6) δ 13.02 (bs, 2H), 8.11–8.05 (m, 2H), 7.95–7.89 (m, 2H), 5.98 (s, 1H). **^{13}C NMR** (101 MHz, DMSO-d_6) δ 166.78, 154.51, 141.39 (q, J = 37.5 Hz), 141.32, 130.55, 129.02, 121.34, 121.30 (q, J = 268.8 Hz), 86.10. **HRMS (ESI):** *m/z* calcd for $C_{11}H_6N_2O_3F_3$ $[M\text{-}H]^-$ 271.0336; found 271.0333.

2.2.3. 4-(4-Acetyl-5-hydroxy-3-(trifluoromethyl)-1H-pyrazol-1-yl)benzoic acid (3)

Compound **2** (2.90 g, 10.65 mmol, 1 equivalent) and triethyl orthoacetate (2.34 mL, 12.79 mmol, 1.2 equivalents) were stirred at 120 °C for 20 min. 96 % *v*/v EtOH (5 mL) and 6 M HCl (0.5 mL) were added and the reaction mixture was mixed at 120 °C for 3 h. Then, the reaction mixture was cooled down, the precipitate was filtered off and dried to give the desired product (55 %) as a light grey solid. **^{1}H NMR** (400 MHz, DMSO-d_6) δ 10.49 (bs, 2H), 8.12–8.06 (m, 2H), 8.04–7.98 (m, 2H), 2.42 (s, 3H). **^{13}C NMR** (101 MHz, DMSO-d_6) δ 188.21, 166.90, 161.09, 141.69, 139.19 (q, J = 37.4 Hz), 130.49, 128.02, 120.90 (q, J = 269.3 Hz), 120.24, 102.54, 26.18. **HRMS (ESI):** *m/z* calcd for $C_{13}H_8N_2O_4F_3$ $[M\text{-}H]^-$ 313.0442; found 313.0441.

2.2.4. 4-(4-Acetyl-5-hydroxy-3-(trifluoromethyl)-1H-pyrazol-1-yl)-N-(prop-2-yn-1-yl)benzamide (LH^2)

Carboxylic acid **3** (1.0 g, 3.18 mmol, 1 equivalent), propargylamine (263 mg, 4.77 mmol, 1.5 equivalents), triethylamine (1.76 mL, 12.7 mmol, 4 equivalents) and DMAP (389 mg, 4.77 mmol, 1 equivalent) were dissolved in DCM (50 mL) and cooled on an ice bath. EDC (911 mg, 4.77 mmol, 1.5 equivalent) was added and the reaction mixture was stirred at room temperature overnight. The reaction mixture was transferred to the separatory funnel and washed with 1 M HCl (4 × 40 mL), brine (30 mL) and dried over Na_2SO_4. Solvents were removed under reduced pressure and the crude product was crystalized from MeOH to give the desired compound (45 %) as a light orange solid. **^{1}H NMR** (400 MHz, DMSO-d_6) δ 9.23 (bs, 2H), 8.98 (t, J = 5.5 Hz, 1H), 8.03–7.90 (m, 4H), 4.07 (dd, J = 5.5, 2.5 Hz, 2H), 3.13 (t, J = 2.5 Hz, 1H), 2.45 (s, 3H). **^{13}C NMR** (101 MHz, DMSO-d_6) δ 188.22, 165.30, 161.03, 140.70, 139.02 (q, J = 37.2 Hz), 130.84, 128.26, 120.97 (q, J = 269.3 Hz), 120.10, 102.38, 81.37, 72.92, 28.56, 26.68. **HRMS (ESI):** *m/z* calcd for $C_{16}H_{11}N_3O_3F_3$ $[M\text{-}H]^-$ 350.0758; found 350.0758.

2.3. Synthesis of complexes

2.3.1. General procedure for the synthesis of lanthanide complexes [Ln(L^1)$_3$(phen)] (Ln = Eu, Sm, Tb)

The β-diketone ligand (**LH^1** or **LH^2**) (3 mmol) and phenanthroline monohydrate (phen·H_2O) (1 mmol) were dissolved in 4 mL of anhydrous ethanol. 1 M NaOH (3 mL, 3 mmol) was added dropwise to the solution and the mixture was heated to 65 °C. The appropriate lanthanide salt (1 mmol) was dissolved in 2 mL of water and was added dropwise to the solution of ligands. After adding the lanthanide salt, the precipitate started to form. The mixture was stirred at 65 °C for 30 min, then overnight at room temperature. The reaction mixture was cooled down, the precipitated product filtered, washed with 50 % EtOH and dried at room temperature.

2.3.2. Synthesis of complex [Eu(L^1)$_3$(phen)]

Complex **[Eu(L^1)$_3$(phen)]** was prepared using the general procedure. $EuCl_3{\cdot}6H_2O$ was used as a source of europium. ^{1}H NMR (400 MHz, $CDCl_3$) δ 10.45 (d, J = 7.8 Hz, 2H), 9.93 (s, 2H), 8.94 (apps, 2H), 8.48 (d, J = 7.8 Hz, 2H), 7.50–7.34 (m, 6H), 6.93–6.82 (m, 6H), 4.80 (d, J = 2.4 Hz, 6H), 3.13 (s, 3H), 2.62 (t, J = 2.4 Hz, 3H).

2.3.3. Synthesis of complex [Sm(L^1)$_3$(phen)]

Complex **[Sm(L^1)$_3$(phen)]** was prepared using the general procedure. $SmCl_3{\cdot}5H_2O$ was used as a source of samarium. ^{1}H NMR (400 MHz, $CDCl_3$) δ 9.58–9.50 (m, 2H), 8.06 (d, J = 8.0 Hz, 2H), 7.94–7.87 (m, 6H), 7.61 (dd, J = 8.1, 4.4 Hz, 2H), 7.48 (apps, 2H), 7.37 (s, 3H), 6.96–6.88 (m, 6H), 4.72 (d, J = 2.4 Hz, 6H), 2.54 (t, J = 2.4 Hz, 3H). Anal. Calcd for $C_{51}H_{32}F_9N_2O_9Sm$ (%): C, 53.82; H, 2.83; N, 2.46. Found: C, 53.23; H, 2.36; N, 2.49.

2.3.4. Synthesis of complex [Tb(L^1)$_3$(phen)]

Complex **[Tb(L^1)$_3$(phen)]** was prepared using the general procedure. $Tb(NO_3)_3{\cdot}5H_2O$ was used as a source of terbium.

2.3.5. Synthesis of complex [Tb(L^2)$_3$(phen)]

Complex **[Tb(L^2)$_3$(phen)]** was prepared using the general procedure. $Tb(NO_3)_3{\cdot}5H_2O$ was used as a source of terbium. Anal. Calcd for $C_{60}H_{41}F_9N_{11}O_9Tb$ (%): C, 51.85; H, 2.97; N, 11.08. Found: C, 51.28; H, 2.30; N, 11.07.

2.3.6. General procedure for copper-catalyzed azide-alkyne cycloaddition reaction between complex and (3-azidopropyl)triethoxysilane

The appropriate lanthanide complex (1 mmol) and (3-azidopropyl) triethoxysilane (3.1 mmol, 3.1 equiv) were dissolved in DCM (1 mL). Catalyst tris(triphenylphosphine)copper(I) bromide (0.05 mmol, 0.05 equiv) was added to the solution and DCM was evaporated in the stream of argon gas. The reaction mixture was kept at 40 °C overnight. The product was used in the next step without any further purification. In the meantime, the product was stored at −20 °C in an inert atmosphere [33].

2.4. Crystallization and X-ray diffraction

The europium and terbium complexes were dissolved in glass vials with a small amount of either chloroform or dichloromethane, the solution was layered with hexane, capped with cotton and left for three days at room temperature. The samarium complex was dissolved in a glass vial with a small amount of chloroform, the solution was layered with heptane, capped with cotton and left for three days at room temperature.

Data from single crystals were collected at 150 K on a SuperNova diffractometer with Atlas detector using CrysAlis software with monochromated Mo Kα (0.71073 Å) or Cu Kα (1.54184 Å) radiation source [Oxford Diffraction Ltd., CrysAlis PRO, Yarnton, Oxfordshire, England, 2011]. The initial structural models were solved with direct methods implemented in SHELXT using the *Olex*2 v1.5 graphical user interface [34]. A full-matrix least-squares refinement on F^2 magnitudes with anisotropic displacement parameters for all non-hydrogen atoms using *Olex*2 [34] was performed. All non-hydrogen atoms were refined anisotropically, while hydrogen atoms were placed at calculated positions and treated as riding on their parent atoms. Details on the crystal data, data acquisition and refinement are presented in Table S1. The crystals used in the analysis are presented in Fig. S11. Mercury [35] software was used to prepare the figures. CCDC 2447474–2447476 contain the supplementary crystallographic data for this paper. These data can be obtained free from The Cambridge Crystallographic Data Centre via https://www.ccdc.cam.ac.uk/data_request/cif.

2.5. Preparation of PMMA-siloxane silica coating

2.5.1. Synthesis of PMMA-siloxane silica solution

The PMMA-siloxane silica solution was synthesized by mixing two separately prepared reaction mixtures according to adjusted protocols from the literature [25–28]: i) copolymerized MMA/MAPTMS sol (Sol 1) and ii) solution of silica precursors (hydrolyzed TEOS, Sol 2). Sol 1 was prepared from 0.027 mol BPO, 0.33 mol MAPTMS and 2.67 mol MMA and THF was added as a solvent while stirring. The copolymerization process between MMA and MAPTMS in the presence of BPO was performed at 70 °C in a closed 50 mL laboratory reactor (EasyMax 102 system, Mettler Toledo). After copolymerization for 4 h, the reactor was

cooled down to room temperature with a cooling rate 10 °C/min. In the meantime, the inorganic Sol 2 was prepared in a separate flask from 0.66 mol TEOS, 1.75 mol ethanol and 3.5 mol acidified water (pH adjusted to 1 with nitric acid) followed by mixing for 15 min at ambient temperature. The Sol 2 was then added dropwise into Sol 1 during vigorous mixing for 1 h at ambient temperature to obtain the final PMMA-siloxane silica solution. 15 mL of the final solution was further diluted with 30 mL THF and stirred (volume ratio between sol and added THF = 1:2).

2.5.2. PMMA-siloxane silica coating solution with admixed alkoxysilane lanthanide complex

The prepared diluted PMMA-siloxane silica solution was admixed with a dry slurry of alkoxysilane lanthanide complex. The mass/volume ratio of alkoxysilane lanthanide complex vs PMMA-siloxane silica solution was tested from 1/2 to 2/1. In a typical experiment where a high loading of fluorescent lanthanide complex was needed, the mass/volume ratio of alkoxysilane lanthanide complex vs PMMA-siloxane silica solution was 2/1. This was also the maximal solubility of the lanthanide complex in PMMA-siloxane silica solution.

2.5.3. Coating of the glass surface

The prepared PMMA-siloxane silica solution with admixed alkoxysilane lanthanide complex was applied to the prepared spherical disk-shaped glass samples (diameter 1 cm) by drop casting. The two-step deposition of the coating was performed by dropping the first 8 μL of hybrid coating solution with admixed alkoxysilane lanthanide complex and waited to dry at room temperature. Next, a second addition of 4 μL of hybrid coating solution with admixed alkoxysilane lanthanide complex was dropped to the primary coating and waited again to dry at room temperature. For control samples without lanthanides, the same procedure has been applied but only without admixing alkoxysilane lanthanide complex (i.e., control glass coating) into PMMA-siloxane silica solution. After complete deposition, the samples rested at room temperature for an additional 30 min for significant drying of THF, and then the coated glasses were thermally cured in the oven at 120 °C for 20 min. Curing at higher temperatures was not recommended due to stability issues of the lanthanide complex.

2.5.4. Characterisation of control and lanthanide-loaded coatings

The chemical composition of the PMMA-siloxane silica coating was performed on coatings deposited by drop casting on aluminium sheets (to avoid the presence of bands related to SiO_2 in the glass substrate). Two coatings were studied: with and without the incorporated europium complex. They were evaluated using attenuated total reflectance Fourier transform infrared spectroscopy (ATR-FTIR, ALPHA II, Bruker) to identify functional groups within the coating matrix and provide insights into potential coordination interactions involving the europium complex. Spectra were recorded in transmittance mode over the spectral range of 4000 to 500 cm^{-1}, with a resolution of 4 cm^{-1}, by averaging four consecutive scans to enhance the signal-to-noise ratio.

The surface and structural morphology of the europium-doped PMMA-siloxane silica coatings deposited on aluminium sheets were further examined using a high-resolution field-emission scanning electron microscope (FEI Helios Nanolab 650) equipped with a focused ion beam (FIB) and coupled to an energy-dispersive X-ray spectrometer (EDS; Oxford Instruments X-max SDD, 50 mm^2). To minimize the charging effects of PMMA-siloxane silica coating and enhance imaging quality, the samples were coated with a thin (~a few tens of nanometres) conductive carbon layer before analysis. Top-view SEM images were acquired in secondary electron (SE) mode using the ICE detector (in-column detector for secondary electrons) at an accelerating voltage of 5 kV.

Cross-sectional imaging was performed on FIB-milled samples using a gallium ion (Ga^+) beam on the same instrument. A 0.2 μm thick layer of electron-deposited platinum (Pt) and 1 μm thick layer of ion-deposited Pt was applied over the targeted area prior to milling to protect the surface and ensure structural integrity during ion etching. Subsequent imaging of the cross-sections was carried out in SE mode using the through-the-lens detector (TLD).

Elemental composition was assessed via EDS on selected regions (areas) of both surface and cross-sectional views to verify the distribution of elements representative of the PMMA-siloxane silica coating and the incorporated europium species. Spectral acquisition and data processing were conducted using AZtec software (version 6.1), providing qualitative and semi-quantitative elemental maps and spectra across the analysed areas. Values are given in weight percentage (wt%).

2.6. Lanthanide-loaded silica nanoparticles

2.6.1. Synthesis of fluorescent lanthanide-loaded silica nanoparticles

The Eu-loaded silica nanoparticles (**SiNP-Eu**) were synthesized using the following procedure. In a glass flask, we mixed 100 mL of deionized water, 80 mL of ethanol, and 12 mL of aqueous ammonia. Next, a solution containing 60 mg of **[Eu(L^1)$_3$(phen)] -Si** dissolved in 500 μL of DMSO and 2 mL of ethanol was prepared and filtered through a 0.22 μm syringe filter. The clear filtrate was added to the mixture in the glass bottle. After this addition, the glass flask was placed in a mechanical shaker (IKA KS 260) set to stirring at 200 rpm. After 15 min of shaking, 6 mL of TEOS dissolved in 18 mL of ethanol was added. The formed reaction mixture was left on the mechanical stirring at 200 rpm overnight. The next day, the formed **SiNP-Eu** were sedimented using centrifugation for 3 min at 3000×*g*, which yielded the sediment containing larger particles and aggregates which were discarded. The remaining supernatant was centrifuged for additional 15 min at 7000×*g* which yielded **SiNP-Eu**. The nanoparticles were washed with ethanol, water, and finally redispersed in 10 mL of water to achieve a concentration of 191 mg/mL (**SiNP-Eu**).

The Tb-loaded silica nanoparticles (**SiNP-Tb**) were synthesized using the following procedure. In a glass flask we mixed 100 mL of deionized water, 80 mL of ethanol, and 12 mL of aqueous ammonia. Next, a solution containing 60 mg of **[Tb(L^2)$_3$(phen)] -Si** dissolved in 500 μL of DMSO and 2 mL of ethanol was prepared. Since this Tb-complex solution was clear, there was no need for filtration. After the addition we placed the glass flask in a mechanical shaker (IKA KS 260) set to stirring at 200 rpm. After 15 min of shaking, 6 mL of TEOS dissolved in 18 mL of ethanol was added. The formed reaction mixture was left on the mechanical stirring at 200 rpm overnight. The next day, the formed **SiNP-Tb** were sedimented using centrifugation for 3 min at 3000×*g*, which yielded the sediment containing larger particles which were discarded due to low colloidal stability. The remaining supernatant was centrifuged for 15 min at 7000×*g* which yielded **SiNP-Tb**. The nanoparticles were washed with ethanol, water, and finally redispersed in 10 mL of water to a concentration of 239 mg/mL for **SiNP-Tb**.

The Sm-loaded silica nanoparticles (**SiNP-Sm**) were synthesized using the following procedure. Firstly, a mixture of 100 mL of deionized water, 80 mL of ethanol, and 12 mL of aqueous ammonia was prepared in a glass flask. Next, a solution containing 60 mg of **[Sm(L^1)$_3$(phen)] -Si** dissolved in 500 μL of DMSO and 2 mL of ethanol was prepared and filtered through a 0.22 μm syringe filter. The clear filtrate was added to the mixture in the glass flask. After the addition, we placed the glass flask in a mechanical shaker (IKA KS 260) set to stirring at 200 rpm. After 15 min of shaking, 6 mL of TEOS dissolved in 18 mL of ethanol were added. The formed reaction mixture was left on the mechanical stirring at 200 rpm overnight. The next day, the formed **SiNP-Sm** were centrifuged for 3 min at 3000×*g*, which yielded the sediment containing larger particles and aggregates which had low colloidal stability and were therefore discarded. The remaining supernatant was sedimented using centrifugation for 15 min at 7000 ×*g*. The nanoparticles were additionally washed with ethanol, water, and finally redispersed in 10 mL of water to a concentration of 130 mg/mL for **SiNP-Sm**.

2.6.2. Characterisation of lanthanide-loaded silica nanoparticles

The synthesized lanthanide-loaded silica nanoparticles were characterized using different techniques. The size and morphology of the silica nanoparticles were analysed using transmission electron microscopy on a JEM-2100 microscope (Jeol, Akishima, Japan) at an accelerating voltage of 200 kV. Nanoparticle suspensions were dropped on carbon-coated copper TEM grids (holey type, mesh 250, Ted Pella, Redding, CA, USA) and left to dry in air at room temperature. No additional contrasting agents were used. The size of the nanoparticles was determined by analysing the TEM micrographs using ImageJ software. At least 100 nanoparticle diameter measurements were used to calculate the average particle diameter and standard deviation.

The surface morphology of the silica nanoparticles was observed using scanning electron microscopy on a Verios 4G HP microscope (Thermo Fisher, Waltham, MA, USA) at an accelerating voltage of 5–20 kV. Energy-dispersive X-ray spectroscopy (EDXS) analysis was done using a UltimMax SDD 65 mm^2 spectroscope (Oxford Instruments, Abingdon, UK). Sample solutions were dropped on double-sided carbon tape on aluminium SEM pin stubs (Micro-to-nano, Tappersweg, Netherlands) and left to dry in the air at room temperature. No additional metal sputtering was used on the samples.

Electrokinetic (zeta) potential at different pH values and hydrodynamic size of the nanoparticles were determined on a Litesizer 500 particle analyser (Anton Paar, Graz, Austria) equipped with a Metrohm auto-dosing system (Metrohm, Harisau, CH) in proprietary polycarbonate Omega cuvettes (Anton Paar, Graz, Austria) at 25 °C. The nanoparticle suspensions were diluted to roughly 0.1 mg/mL in 10 mM aqueous potassium chloride solution for measurements.

The fluorescence of the lanthanide-complex-loaded silica nanoparticle suspensions was visually observed using a UV light (NU-8, Benda, Germany) at 366 nm.

2.7. Temperature measurement procedure

Preliminary spectrometric analysis of the temperature sensitivity of fluorescent lanthanide complexes was performed using a multimodal plate reader (Tecan Spark, Männedorf, Switzerland). To evaluate their thermal responsiveness and spectroscopic properties, fluorescence emission spectra of the complexes dissolved in Miglyol 812 were recorded. Temperature-dependent emission behavior was assessed by monitoring changes in fluorescence intensity during a controlled heating cycle from room temperature to approximately 40 °C. Measurements were taken in 5 K increments, with each temperature point held until thermal equilibrium was reached, typically within 10 to 15 min depending on the target temperature.

A fluorescence microspectroscopy (FMS) system, capable of acquiring images with micrometre spatial resolution, was used for thermal imaging and evaluation of the temperature-dependent fluorescence emission spectra of the thermosensitive coatings. The system was built on a Nikon Eclipse Ti2 inverted microscope platform, consisting of the excitation, dichroic and emission filters (BrightLine filters from AHF, Tübingen-Pfrondorf, Germany). The objective with 10× magnification was used in these experiments to provide the high magnification and high spatial resolution required. To achieve precise movement of the cell, a motorised and computer-controlled SCAN IM-series stage (Märzhäuser Wetzlar, Wetzlar, Germany) was used. A CoolLED pE-4000 high-power LED source (CoolLED, Andover, UK) was utilized as the excitation source, with tunable output wavelengths ranging from 365 to 770 nm. The fluorescence light was passed through a narrowband, liquid-crystal tunable filter (LCTF) (Kurios-VB1, Thorlabs, Newton, NJ, USA) covering the 420–730 nm range with approximately 10 nm bandwidth, placed in front of the CMOS camera ZWO ASI183MM-Pro (Suzhou ZWO Co., Suzhou, JS, CN). The temperature-dependent emission spectra in the red region were measured using UV excitation. A step size of 1 nm was selected to provide a more accurate and comprehensive assessment of the emitted fluorescence. The florescence in each spectral band were then processed and analysed using a custom MatLab script. The script was also used to subtract the offset signal from the camera due to the non-uniform transmittance of the LCTF.

Prior to measurements, the fluorescent probe solution was applied to a 12 mm round coverslip. It was spread evenly using an Osilla spin coater (Ossila Ltd., Sheffield, UK) to achieve a uniform coating thickness and allowed to dry. To achieve the desired temperatures, the coated coverslip was placed in a custom 3D-printed plastic temperature control cell to fit on the microscope. The cell consisted of a thermal stack with a copper block containing the k-type thermocouple (Labfacility Limited, South Yorkshire, UK), the TEC1–07110 Peltier element (EVER-REDtronics LTD, Shanghai, SH, CN) and a water-cooled heat sink block mounted on top. The temperature was manually controlled from room temperature to 70 °C. This was done by adjusting the DC supply voltage of the EA-PS 3032-10B DC power supply (Elektro-Avtomatik, Viersen, GER) and monitoring the temperature readings using an Agilent 34970A (Loveland, CO, USA) data acquisition unit equipped with an Agilent 34901A multiplexer module. The aim was to achieve steady-state conditions at a given temperature level and homogeneous temperature distribution within the coated coverslip. Quasi-stationary conditions were typically reached after 15 min, with a temperature step between measurements of 5 °C.

2.8. Live-cell fluorescence imaging procedure

Fluorescence imaging of the silica nanoparticles with Eu (**SiNP-Eu**), Sm (**SiNP-Sm**), and Tb complexes (**SiNP-Tb**) was performed on a custom-built laser-scanning confocal fluorescence microscope (Abberior Instruments) with a 60× water immersion objective (NA 1.2) and a stage-top incubator with 5 % CO_2 set to 37 °C.

The nanoparticles were imaged at a final concentration of 1 mg/mL. For imaging, the nanoparticles were either (A) diluted and imaged in colorless L-15 medium (Gibco) after 30 min to let the particles settle to the bottom of the imaging chamber, or (B) added to LA-4 cells (ATCC) in complete F-12K cell medium and imaged after a day of incubation without prior washing. The complete cell medium consisted of F-12K (Gibco), 15 % FBS (Gibco), 1 % P/S (Gibco), 1 % NEAA (Gibco), and 1 % GlutaMax (Gibco). The cells were cultured according to the manufacturer's guidelines and seeded in 18-wells with a 1.5H glass coverslip bottom (Cellvis) for imaging. Two hours prior to imaging, cells were labelled with 1 μg/mL CellMask Deep Red Plasma Membrane Stain (Invitrogen).

During imaging, the fluorescence was excited with a continuous wave 405 nm laser (800 μW power in the sample plane) and detected at 581–627 nm (for the nanoparticles) and 651–720 nm (for CellMask Deep Red) with an APD detector. The pinhole size was 1.1 AU. For images with 20 μm fields of view, the pixel size was 50 nm, and for images with 5 μm FOV it was 20 nm. A total pixel dwell time of 30 μs was used for imaging.

3. Results and discussion

3.1. Synthesis, crystal structure and spectral properties

The overall strategy for the synthesis involved producing complexes with europium (Eu), terbium (Tb), and samarium (Sm) that contained clickable alkyne functional groups attached to the ligands. These complexes were then tested for their thermal sensitivity, and only the selected ones were incorporated onto glass surfaces or into silica nanoparticles through a prior attachment of silane ether via CuCAA reaction.

Ligands $\mathbf{LH^1}$ and $\mathbf{LH^2}$ were based on well-established ligands, benzoyltrifluoroacetone (BTA) and 1-phenyl-3-trifluoromethyl-4-acyl-5-pyrazolone (PFAP) [36], respectively, with an attached propargyl group. The synthesis of $\mathbf{LH^1}$ began with the reaction between the phenol moiety of 4-hydroxyacetophenone and propargyl bromide, producing propargyl ether **1** (Scheme 1). This intermediate was then converted via

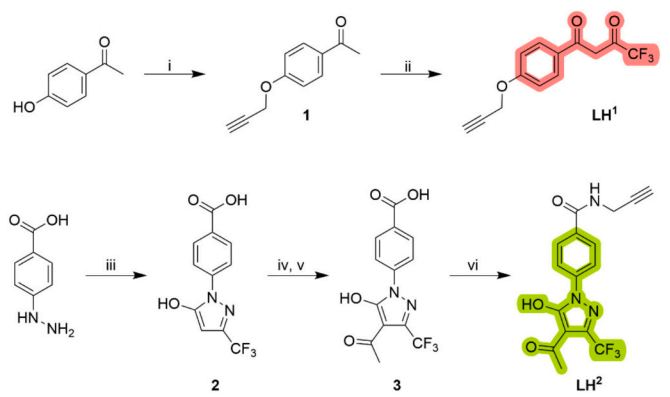

Scheme 1. Reagents and conditions: (i) propargyl bromide, K_2CO_3, ACN, 70 °C; (ii) ethyl 2,2,2-trifluoroacetate, NaH, THF, 0 °C; (iii) ethyl 4,4,4-trifluoroacetoacetate AcOH, 115 °C; (iv) triethyl orthoacetate, 110 °C; (v) 6 M HCl, EtOH, 110 °C; (vi) propargylamine, EDC, DMAP, Et_3N, DCM, RT. BTA and PFAP scaffolds are highlighted in red and green, respectively.

Claisen condensation to 1,3-diketone **LH^1** [37].

The synthetic route for ligand **LH^2** started with the reaction between ethyl 4,4,4-trifluoroacetoacetate and 4-hydrazinobenzoic acid to form pyrazole **2** [38], to which a trifluoroacetate group was introduced [39], yielding compound **3**. In the final step, the carboxylic acid group of compound **3** was coupled with propargylamine to produce the final ligand, **LH^2** (Scheme 1).

Complexes were synthesized by reacting ligands **LH^1** or **LH^2**, phenanthroline, and the appropriate lanthanide salt in a mixture of water and ethanol, with sodium hydroxide used to adjust the pH (Scheme 2) [40]. Europium (Eu), samarium (Sm), and terbium (Tb) salts were selected because their complexes emit in the visible range. The BTA-based ligand **LH^1** was selected for complexes with Eu and Sm, yielding **[Eu(L^1)$_3$(phen)]** and **[Sm(L^1)$_3$(phen)]**, respectively. However, the BTA ligand is unsuitable for Tb due to the low energy of its excited triplet state [41,42]. Despite this, we synthesized **[Tb(L^1)$_3$(phen)]**, which, as expected, displayed very weak emission. To improve Tb luminescence, we employed the established pyrazole-based ligand **LH^2**, forming **[Tb(L^2)$_3$(phen)]** [36]. In the final step, the complexes were functionalized with reactive triethoxysilane moieties via CuAAC reaction with (3-azidopropyl)triethoxysilane. Due to the moisture sensitivity and tendency of the triethoxysilane moiety to hydrolyse, the product was not purified and was instead used directly in the subsequent reaction step.

In these complexes, ligands **LH^1** and **LH^2** act as antennas, absorbing light and transferring the energy to the central lanthanide ion. Phenanthroline was used as an auxiliary ligand to displace water molecules coordinatively bonded to the lanthanide ion, significantly enhancing the complexes' photophysical properties [43].

All crystallized lanthanide complexes display the expected square antiprismatic geometry for 8-coordinated metal ions typical of lanthanide complexes bearing three β-diketonate ligands and a nitrogen bidentate ligand such as 1,10-phenanthroline (Fig. 1). The europium complex crystallizes with two complex molecules in the asymmetric unit which are distinguished by different rotational positions of the oxypropynyl group and the terbium complex structure contains a chloroform-*d* solvate molecule. All bond lengths of the coordinated ligands fall within the range of reported structures with Ln-O bond lengths between 2.31 and 2.39 Å and the and the Ln-N bonds between 2.52 and 2.60 Å.

Before reacting the complexes with (3-azidopropyl)triethoxysilane, we tested their temperature sensitivity by measuring the fluorescence spectra across a wide optical window (Fig. 2). The testing was conducted in a solution of Miglyol 812, a medium comprising glycerol triesters of caprylic and capric acid, chosen for its low vapor pressure to minimize evaporation during the experiment. Preliminary spectrometric analysis of the complexes dissolved in Miglyol 812 revealed that only the **[Eu(L^1)$_3$(phen)]** exhibited significant temperature-dependent changes in fluorescence emission. In contrast, the **[Tb(L^2)$_3$(phen)]** and **[Sm(L^1)$_3$(phen)]** showed insufficient sensitivity to temperature variations, rendering them unsuitable for further development. Additionally, the **[Tb(L^2)$_3$(phen)]** required excitation wavelengths below 350 nm, which are rarely included in commercial fluorescence microscopes. Given these findings, we selected the **[Eu(L^1)$_3$(phen)]** as the most suitable for incorporation into PMMA-siloxane silica coatings and subsequently into silica nanoparticles.

3.2. Characteristics of Eu-loaded PMMA-siloxane silica coating

3.2.1. FTIR coating characterisation

ATR-FTIR spectroscopy investigated the structural characteristics of PMMA-siloxane silica coatings synthesized with and without incorporating a europium complex Fig. 3. The recorded spectra provide insight

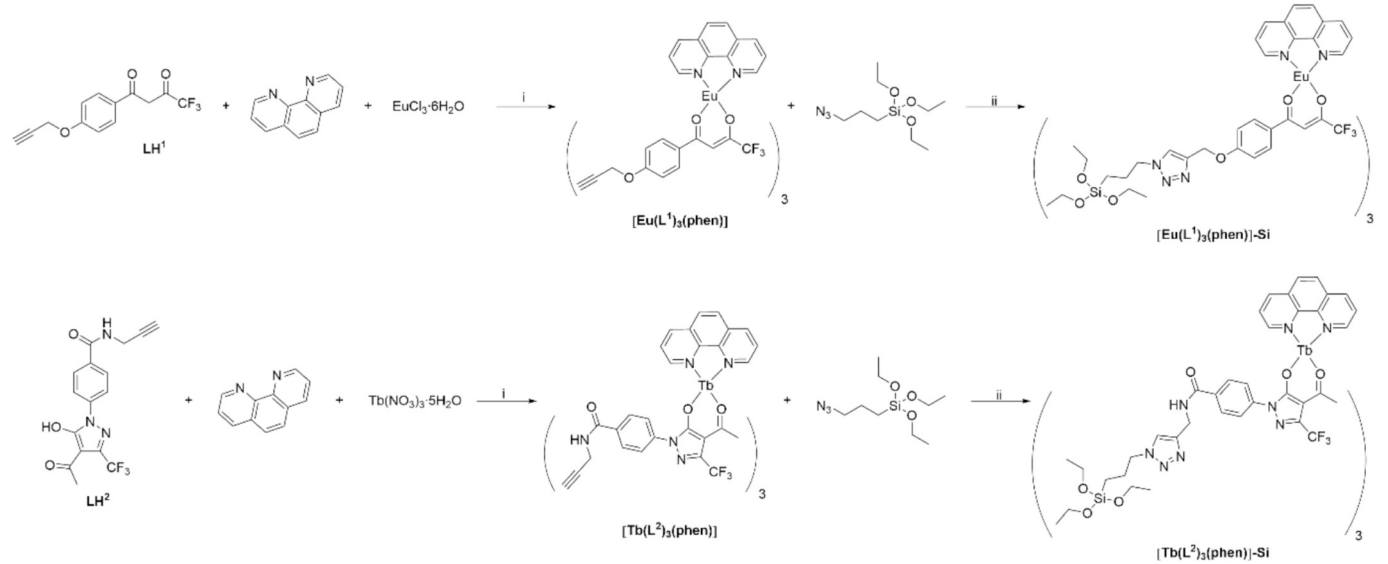

Scheme 2. Reagents and conditions: (i) NaOH, EtOH/H_2O, 65 °C; (ii) tris(triphenylphosphine)copper(I) bromide, DCM, 40 °C. **[Sm(L^1)$_3$(phen)]-Si** and **[Tb(L^1)$_3$(phen)-Si** were synthesized according to the scheme for **[Eu(L^1)$_3$(phen)]-Si**, starting from $SmCl_3{\cdot}5H_2O$ and $Tb(NO_3)_3{\cdot}5H_2O$.

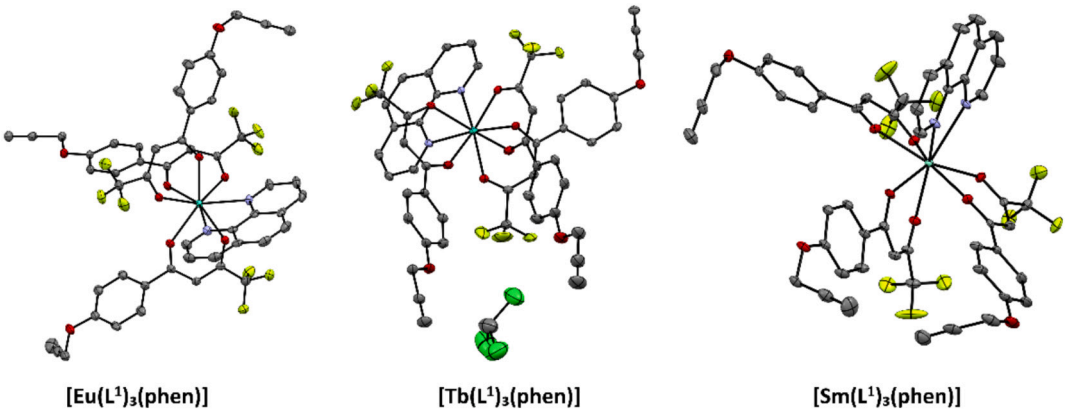

Fig. 1. Crystal structures of **[Eu(L^1)$_3$(phen)]**, **[Tb(L^1)$_3$(phen)]** and **[Sm(L^1)$_3$(phen)]**. Thermal ellipsoids are drawn at 35 % probability. Hydrogen atoms are omitted for better clarity. Atom types are represented using default colors in Mercury (C – grey, O – red, N – blue, F – yellow, Ln – cyan, Cl – green). (For interpretation of the references to colour in this figure legend, the reader is referred to the web version of this article.)

into the presence and potential interaction of organic and inorganic components within the matrix and the influence of the europium species on the coating composition.

Both FTIR spectra display characteristic bands associated with the PMMA-siloxane silica coating network [28,29,44]. A broad band centred around 3430 cm^{-1} is observed in both coatings, corresponding to O—H stretching vibrations. This absorption may originate from residual hydroxyl groups within the silica framework, which remains present after thermal curing at 120 °C. To minimize the presence of O—H, the coatings need to be cured at higher temperatures, but the limit is ~200 °C [27]. The intensity of this wide band is significantly lower in the presence of the **[Eu(L^1)$_3$(phen)] -Si** due to the greater interaction of the coating matrix and functional (ethoxy) groups in the **[Eu(L^1)$_3$(phen)] -Si** complex, as presented in Scheme 2. In the region between 2950 and 2850 cm^{-1}, distinct bands attributed to C—H stretching vibrations of methyl and methylene groups are detected, arising from the organic components such as methylmethacrylate (MMA) and 3-(trimethoxysilyl)propyl methacrylate (MAPTMS).

The most prominent absorption feature in both spectra is located at 1720 cm^{-1} related to C═O bands and 1632 related to C═C bands, Fig. 3. Bands at 1062 cm^{-1} and 1045 cm^{-1}, attributed to the asymmetric stretching vibration of the Si—O—Si network, indicative of a well-condensed siloxane backbone [28,29]. A secondary shoulder or overlapping band at 1235 and 1291 cm^{-1} is assigned to Si—O—C or C—O—C stretching, confirming the presence of covalent linkages between the organic and inorganic domains.

Upon doping with the europium complex, several spectral changes are evident. Most notably, the doped sample exhibits increased absorbance intensity at 1566 and 1593 cm^{-1}. This region is typically associated with bending modes of CH_2/CH_3 groups and aromatic ring vibrations [45,46], as presented in **[Eu(L^1)$_3$(phen)] -Si** in Scheme 2. The enhanced intensity and possible slight band shifts in this region suggest the introduction of new chemical environments due to the europium complex, likely related to coordination interactions between Eu^{+3} ions and electron-donating groups present in the organic network.

The Eu-doped coating also exhibits band intensity and profile changes in the lower wavenumber region (600–800 cm^{-1}), with an intensive band at 782 cm^{-1}. These modifications could reflect Eu—O vibrations or structural perturbations of the inorganic siloxane network induced by incorporating the europium species. The Si—O—Si band around 1040–1100 cm^{-1} also exhibits slight variations in shape and intensity, which may be attributed to crosslinking effects or changes in the siloxane condensation degree upon complex incorporation.

These FTIR spectral differences confirmed the efficient polymerisation of PMMA-siloxane silica without and with **[Eu(L^1)$_3$(phen)] -Si**. The observed changes are consistent with the coordination of europium to oxygen-rich sites within the network, which may influence both the inorganic framework and the surrounding organic domains. These findings align with prior studies on similar hybrid sol-gel systems, where dopants such as metal complexes interacted with silanol groups and organic components, leading to modifications in the local bonding environment and the overall network structure.

3.2.2. Surface morphology and cross-sectional structure characterisation using scanning electron microscopy

The surface morphology and internal structure of the PMMA-siloxane silica coating doped with europium complex were analysed using high-resolution field-emission scanning electron microscopy (FE-SEM), complemented by focused ion beam (FIB) milling and energy-dispersive X-ray spectroscopy (EDS), Fig. 4.

Fig. 4A shows a top-view SEM image of PMMA-siloxane silica coating. The surface appears continuous and relatively smooth, interspersed with homogeneously distributed micro- and nanoscale domains. Continuous surface, and a compact internal structure (Fig. 4B), suggest successful and uniform integration of the europium complex within the PMMA-siloxane silica matrix. Such morphology supports forming a dense, cohesive network, indicating good film-forming properties and mechanical stability [28,29,44]. There are only seen valleys along the surface that remain at the surface after solvent (THF) and side products (alcohols, water) evaporation while thermal curing the coatings at 120 °C. As presented in the inserted image, the diameter can be from a few hundred nanometres up to 1 um. Despite the presence of these valleys, the coating is without any cracks.

Fig. 4B presents the cross-sectional view of the same coating obtained via FIB milling and analysed in SE mode using the TLD detector, allowing for high-resolution visualization of internal coating morphology, layer uniformity and coating thickness. The cross-section reveals a compact, coating structure with a measured thickness above 4 μm (from the top). The coating exhibits no signs of valleys seen from top-view imaging and no delamination, microcracks, or interfacial voids, indicating strong adhesion to the aluminium substrate and excellent structural coherence. These are important parameters for ensuring the durability of Eu-doped coating. There are only seen some brighter areas of a few tens of nanometres in size, indicating silicate domains in PMMA-siloxane silica coatings [28,29,44].

Elemental analysis via EDS was performed on selected regions marked with dashed squares in both the surface and cross-sectional images. The obtained spectra and values in the Tables (as part of Fig. 3) confirmed the great amount of silicon (Si), oxygen (O), and carbon (C), characteristic of the PMMA-siloxane silica matrix. Notably, distinct signals attributable to europium were also detected (Eu = 9.1 wt %, F = 4.0 wt% and N 1.8 wt%), confirming the incorporation of the **[Eu**

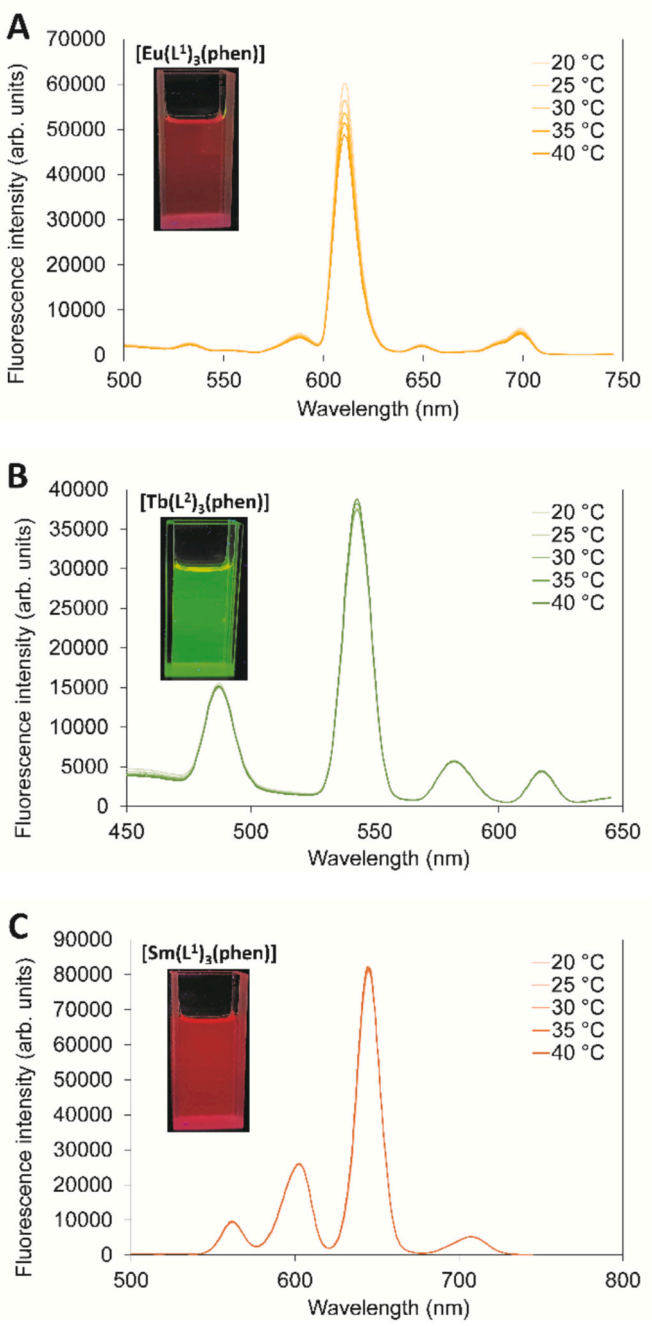

Fig. 2. The emission spectra of the complexes: (A) **[Eu(L^1)$_3$(phen)]**, (B) **[Tb(L^2)$_3$(phen)]**, (C) **[Sm(L^1)$_3$ (phen)]** were recorded in Miglyol 812, with a concentration of 0.1 mM for the europium (Eu) and terbium (Tb) complexes, and 1 mM for the samarium (Sm) complex. The excitation wavelengths were 370 nm for **[Eu(L^1)$_3$(phen)]**, 330 nm for **[Tb(L^2)$_3$(phen)]**, and 360 nm for **[Sm(L^1)$_3$(phen)]**.

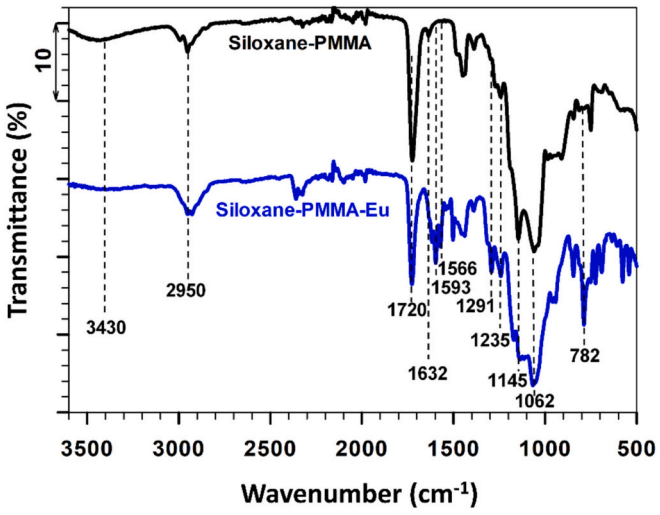

Fig. 3. ATR-FTIR spectra of PMMA-siloxane silica coatings synthesized without and with **Eu(L^1)$_3$(phen)]-Si**.

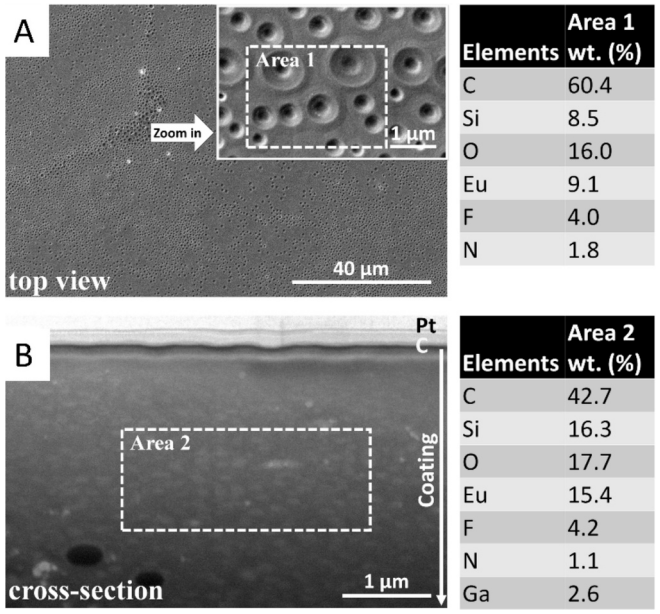

Elements	Area 1 wt. (%)
C	60.4
Si	8.5
O	16.0
Eu	9.1
F	4.0
N	1.8

Elements	Area 2 wt. (%)
C	42.7
Si	16.3
O	17.7
Eu	15.4
F	4.2
N	1.1
Ga	2.6

Fig. 4. Surface morphology and internal structure of the PMMA-siloxane silica coating doped with europium complex. (A) The top view SEM image was performed in secondary electron (SE) mode using an ICE detector of PMMA-siloxane silica coating synthesized with the europium complex. (B) A cross-sectional FIB-SEM image of the same coating performed in SE using a TLD detector. Tables summarizing the results of energy-dispersive X-ray spectroscopy (EDS) performed on selected areas in a and b, marked with dashed squares.

(L^1)$_3$(phen)]-Si into the coating. A similar composition was also noticed in the coating cross-section with a similar amount of **[Eu(L^1)$_3$(phen)]-Si** (Eu = 15.4 wt%, F = 4.2 wt% and N 1.1 wt%). It is important to note that the EDS spectral peaks of europium (Eu Mα) overlap with those of gallium (Ga Lα) at ~1.12 keV. Since gallium was used as the ion source during FIB milling, its presence in the cross-sectional spectrum must be interpreted cautiously. However, Eu was also detected on the coating surface, where gallium contamination is absent, confirming its incorporation. The **[Eu(L^1)$_3$(phen)]-Si** is evenly distributed in all the coating regions (without any domains), as presented in the FIB-SEM/EDS mapping, Fig. S12.

These findings align well with the ATR-FTIR results, which showed coordination interactions within the coating network. The observed dense structure and elemental uniformity are consistent with previously reported PMMA-siloxane silica systems doped with rare earth elements, where similar morphologies were linked to high mechanical integrity, chemical stability, and optical responsiveness [45–47].

The obtained coating thickness (~14 µm) significantly exceeds that of dip-coated PMMA-based sol-gel coatings (~2–4 µm), but the increased thickness did not compromise the film's integrity or homogeneity [28,29,44]. Under UV light exposure, the Eu-loaded coatings emitted intense red luminescence (Fig. 5A). SEM and EDS

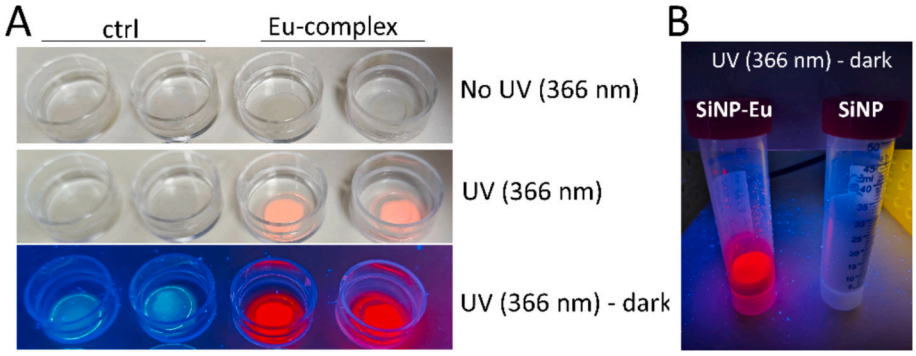

Fig. 5. (A) Photographs of the fluorescence from the lanthanide-complex containing PMMA-siloxane silica coating (Eu-complex) and the control PMMA-siloxane silica coating without dye (ctrl). Top row shows no UV exposure, middle row - an exposure of UV light (NU-8, Benda, Germany, 366 nm) and bottom row - the same settings in the dark. (B) Photographs of the fluorescence of the lanthanide-complex-containing silica nanoparticle suspension **SiNP-Eu** and control silica nanoparticles without dye (**SiNPs**) were taken under UV light (NU-8, Benda, Germany) at 366 nm.

characterisation confirmed that the coating maintained structural cohesion embedding the europium complex, highlighting its robustness and scalability for advanced applications such as luminescent thermometry or optical sensing. Additionally, the coatings proved stable when submerged in water, with no leaching or solvent-induced effects on emission observed (Fig. S13).

3.3. Characteristics of lanthanide-loaded silica nanoparticles

The lanthanide-complex containing silica nanoparticles (Fig. 5B and Fig. 6) were synthesized using the well-established Stöber sol-gel silica synthesis method, based on the hydrolysis and condensation of tetraethoxysilane (TEOS) in a mixture of water, ethanol, and aqueous ammonia as the base catalyst. Interestingly, the solubility of the lanthanide-complex in the mixture of ethanol and DMSO was different depending on the lanthanide in the complex, where the **[Sm (L^1)$_3$(phen)] -Si** and **[Eu(L^1)$_3$(phen)] -Si** did not dissolve completely and the solution remained cloudy despite intense ultrasonication. Therefore, the Sm- and Eu-complex solutions were filtered through a 0.22 μm syringe filter prior adding it to the reaction mixture. In contrast, the **[Tb (L^2)$_3$(phen)] -Si** dissolved completely in ethanol and DMSO and formed a clear solution without the need for filtration.

The synthesized nanoparticles were relatively monodispersed, as shown in Fig. S14, with mean hydrodynamic sizes of (208.4 ± 43.6) nm, (185.7 ± 32.5) nm, and (142.2 ± 15.3) nm for **SiNP-Eu**, **SiNP-Sm**, and **SiNP-Tb**, respectively. Zeta potential measurements show that all three nanoparticle samples have similar isoelectric points between pH 3 and 4. Finally, all three samples showed high negative zeta potential values at higher pH values, reaching – 40 mV at approximately pH 6.

3.4. Temperature-dependent fluorescence spectra of PMMA-siloxane silica coating with [Eu(L^1)$_3$(phen)]-Si

The peak-normalized fluorescence spectrum of an Eu-loaded coating at room temperature is shown in Fig. 7. The absorption and fluorescence spectra do not overlap and show a large Stokes shift. For this particular complex, the reddish Eu^{3+} emission spectrum typically shows bands associated with $^5D_0 \rightarrow {}^7F_J$ transitions (J = 0–4).

Therefore, for our investigation, we focused on two prominent peaks at about 589 and 611 nm. Their levels are separated by a very narrow energy gap of $\Delta E = 611\ cm^{-1}$, corresponding to the $^5D_0 \rightarrow {}^7F_1$ and $^5D_0 \rightarrow {}^7F_2$ electron transitions, respectively. As shown in Fig. 8A, the fluorescence intensity of the most prominent peak at 611 nm decreases significantly over the observed temperature range, and the fluorescence

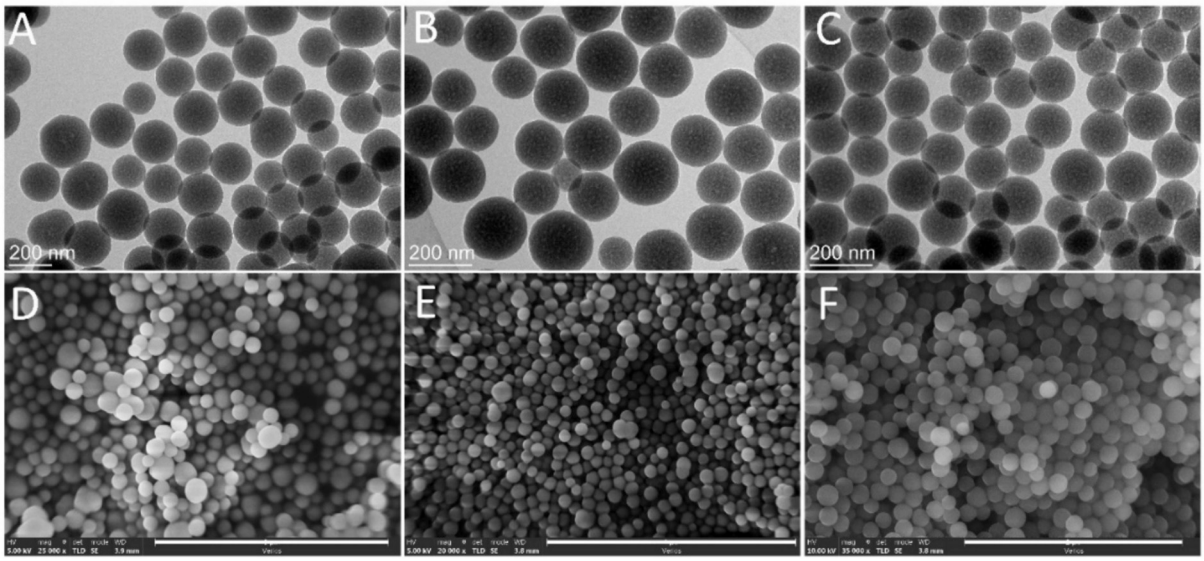

Fig. 6. Transmission electron microscopy (TEM) images (A-C) of Eu-loaded silica nanoparticles – **SiNP-Eu** (A), Sm-loaded silica nanoparticles – **SiNP-Sm** (B), and Tb-loaded silica nanoparticles – **SiNP-Tb** (C). Scanning electron microscopy (SEM) images (D–F) of Eu-loaded silica nanoparticles – **SiNP-Eu** (D), Sm-loaded silica nanoparticles – **SiNP-Sm** (E), and Tb-loaded silica nanoparticles – **SiNP-Tb** (F). Size bars are 3 μm for D), 4 μm for E), and 2 μm for F).

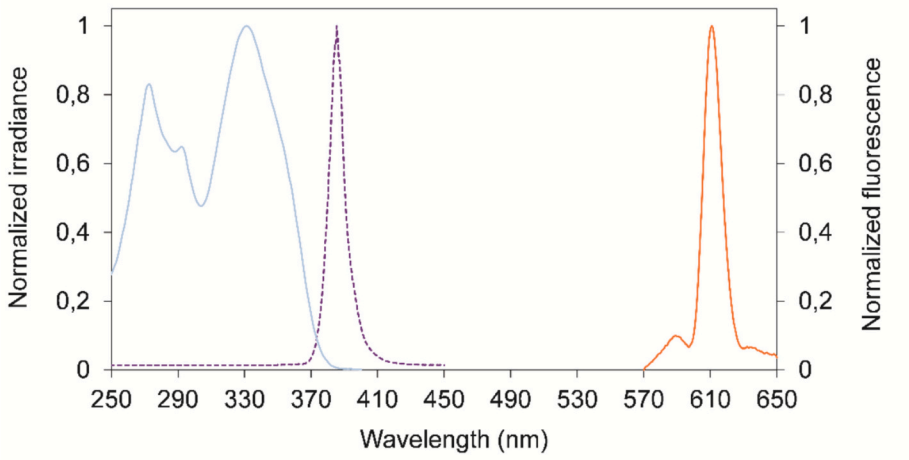

Fig. 7. Peak-normalized absorption and fluorescence spectra (solid lines) of the Eu-loaded coating measured at room temperature using the FMS system. The normalized irradiance spectrum of the LED source, peaking at 385 nm, is shown as a violet dashed line. (For interpretation of the references to colour in this figure legend, the reader is referred to the web version of this article.)

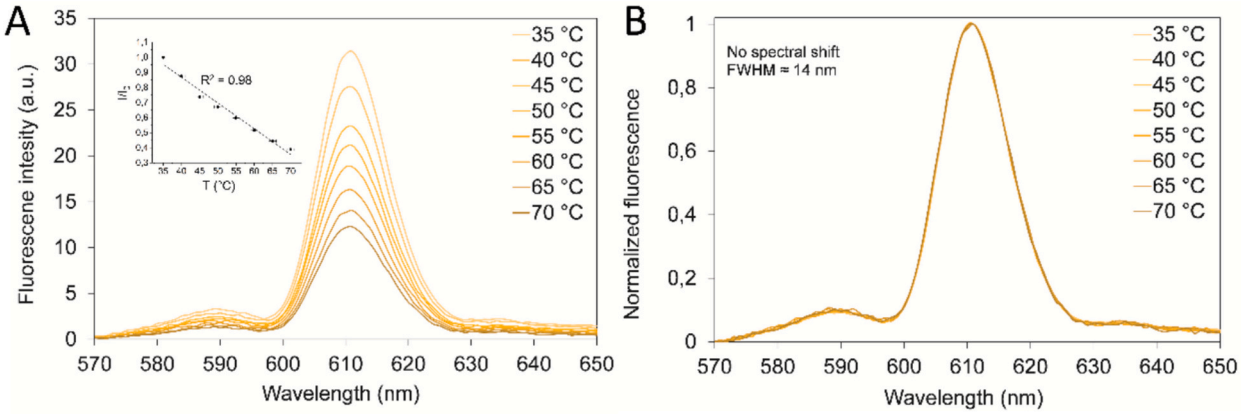

Fig. 8. Temperature-dependent fluorescence spectra of Eu-loaded coating. (A) Evolution of the emission spectra of an Eu-loaded coating as a function of temperature during the heating cycle. An inset presents the temperature sensitivity of fluorescence intensity of an Eu-loaded coating. (B) Normalized temperature-dependent fluorescence spectra shown in (A).

spectrum has a Full Width Half Maximum (FWHM) bandwidth of 14 nm. The temperature sensitivity of fluorescence intensity was determined through linear least-squares fitting of data between 35 °C and 70 °C, yielding a value of ≈ −1.7 % per Kelvin relative to the intensity at 35 °C (Fig. 8A, Inset). Goodness of fit was confirmed with the R-squared of 0.98. Normalized spectra to the peak values show that there is no blue or red shift, i.e. no shift to the left or right of either emission peak (Fig. 8B). The spectra also show no significant spectral broadening or narrowing at elevated temperatures. On the other hand, there is a slight decrease in the fluorescence intensity of the peak at 589 nm. From a practical point of view, this is good for ratiometric temperature measurement, where the ratio of intensities between both peaks is independent of several external variables, such as excitation intensity fluctuation, concentration changes, photobleaching etc. However, the sensitivity for ratiometric temperature sensing is rather poor as the two corresponding peaks follow the similar trend with the temperature. However, it should be noted that the temperature sensitivity is negatively affected as the two corresponding peaks follow the same trend of decreasing fluorescence intensity. In addition to the above measurements, a pronounced photobleaching effect of 10–15 % was observed throughout heating cycle measurements (Fig. S15), underscoring the need for improved photostability to fully realise the potential of this Eu-loaded coating in sensing applications. This effect was taken into account for normalization of the spectra presented in Fig. 8A. Photobleaching clearly shows that the fluorescence emission of the thermosensitive coating is adversely affected by prolonged exposure to UV light, but in the context of typical short exposure times (< 1 s) with similar irradiance in e.g. biosensing applications, the effect of photobleaching becomes less relevant.

3.5. *Fluorescence imaging of live lung epithelial cells*

To test the suitability of the silica nanoparticles with Eu, Sm, and Tb complexes for fluorescence imaging in biological samples, we imaged them with a laser-scanning confocal fluorescence microscope using 405 nm excitation in colorless cell media. Despite the homogeneous size distribution of the particles, their fluorescence intensity was very heterogeneous (Fig. 9 and Fig. S16). The fluorescence intensity of certain particles in both **SiNP-Eu** and **SiNP-Sm** was notably larger than cell's native autofluorescence. Fairly high excitation laser powers were needed to achieve reasonable fluorescence signal from the nanoparticles, partially due to the mismatch between the excitation spectra of Eu and Sm and the lowest available laser on our microscope (405 nm). We expect this to be the case for many standard laser-scanning optical microscopes as well, as they rarely include excitation lasers with lower wavelengths. Negligible fluorescence was observed from sample **SiNP-Tb**, which was expected due to its low excitation at 405 nm.

Next, we imaged the lanthanide-loaded silica nanoparticles after a 1-

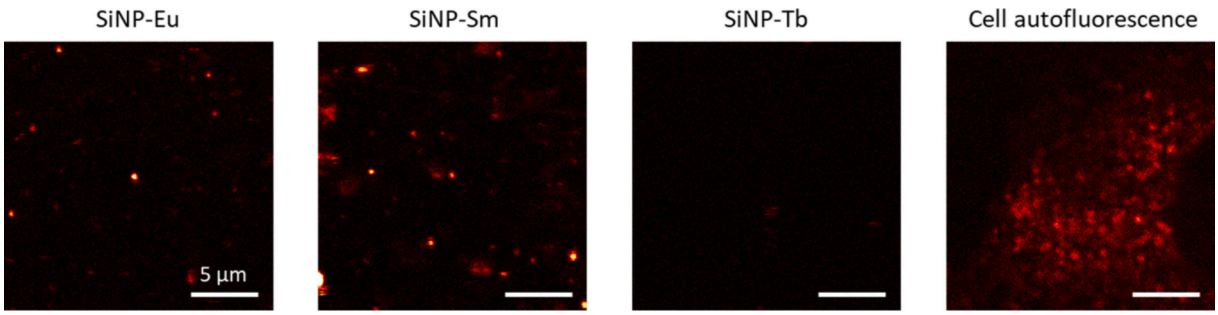

Fig. 9. Left three images: Fluorescence micrographs of silica nanoparticles with embedded complexes in colorless cell medium L-15. Far right: the autofluorescence of a non-labelled live LA-4 cell for comparison. Imaging parameters and contrasting were the same for all images to enable comparison of the intensities.

day incubation with live lung epithelial cells (cell line LA-4) to evaluate their potential use as intercellular thermometers. As shown on Fig. 10 and Fig. S17, **SiNP-Eu** was mostly observed outside cells, and rare internalized particles were observed. The fluorescence signal of **SiNP-Sm** and **SiNP-Tb** was too dim compared to autofluorescence for any conclusions regarding their internalisation. Encouragingly, we did not observe any visible cytotoxic effects in the nanoparticle-exposed cells after the 1-day exposure, i.e. oddly-shaped nuclei or blebbing. However, more thorough testing should be performed to determine the live-cell compatibility of these samples. Some bleaching of the complexes was observed after long continuous imaging of a region of interest in all samples. This could be at least partially the consequence of the large excitation powers (almost 1 mW) required to obtain the images. Thus, to successfully use these complexes as intercellular thermometers, their internalisation and brightness should be improved, and their cytotoxicity evaluated in more detail. For instance, internalisation could be improved by surface functionalisation of the particles [48], and the brightness of the particles by increasing the concentration of lanthanides per particle. We would also expect more internalisation of particles in professional phagocytes (for example, macrophages and monocytes).

4. Conclusions

In this study, we successfully developed and characterized silane-modified lanthanide complexes for integration into PMMA-siloxane silica coatings and silica nanoparticles, demonstrating their potential for high-resolution temperature sensing and live-cell labeling. The europium-based complex, selected for its promising thermal response, was functionalized via CuAAC reaction with silyl ethers, enabling its incorporation into a PMMA-siloxane silica matrix and silica nanoparticles. The developed temperature-sensitive coatings exhibited strong chemical stability, mechanical robustness, and high spatial resolution, making them highly suitable for non-invasive thermal sensing applications. Fluorescence microscopy confirmed their responsiveness to temperature variations, with a sensitivity of ≈ -1.7 % per Kelvin between 35 °C and 70 °C. While some photobleaching was observed, the materials maintained sufficient stability under optimized conditions, indicating their viability for thermal imaging. Additionally, europium-loaded silica nanoparticles demonstrated some internalisation in lung epithelial (LA-4) cells, as confirmed by confocal microscopy, and their signal was distinguishable from the cell autofluorescence. These findings highlight their potential as bioimaging probes for cellular applications, particularly in environments requiring precise fluorescence-based temperature monitoring. Importantly, no visual cytotoxic effects were observed, further supporting their suitability for biomedical applications. Although challenges related to photostability remain, our results establish a strong foundation for the further development of lanthanide-based luminescent materials for both thermal sensing and bioanalytical applications. Future work will focus on enhancing photostability and optimizing ligand structures to extend their usability in long-term imaging and sensing environments.

CRediT authorship contribution statement

Ivan Sedmak: Writing – original draft, Methodology, Investigation, Formal analysis, Conceptualization. **Aljoša Bolje:** Writing – review & editing, Investigation. **Jakob Kljun:** Writing – original draft, Investigation, Formal analysis. **Rok Podlipec:** Writing – review & editing,

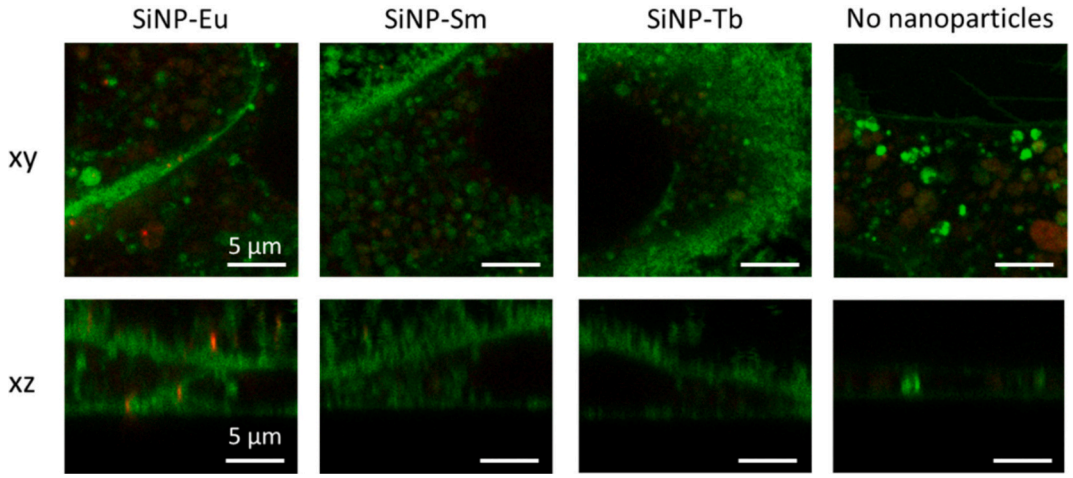

Fig. 10. Fluorescence micrographs of silica nanoparticles with embedded complexes (shown in red) in live LA-4 cells (cell membranes labelled with CellMask Deep Red, shown in green). Imaging parameters and contrasting were kept constant for all images to enable comparison. XZ crossections were imaged across the middle of the acquired XY range. (For interpretation of the references to colour in this figure legend, the reader is referred to the web version of this article.)

Investigation, Formal analysis. **Hana Kokot:** Writing – original draft, Investigation, Formal analysis. **Sebastjan Nemec:** Writing – original draft, Investigation. **Slavko Kralj:** Writing – original draft, Investigation, Funding acquisition, Formal analysis. **Peter Rodič:** Writing – original draft, Investigation, Formal analysis. **Iztok Golobič:** Writing – review & editing, Methodology, Funding acquisition, Conceptualization. **Stane Pajk:** Writing – original draft, Investigation, Funding acquisition, Conceptualization.

Declaration of competing interest

The authors declare that they have no known competing financial interests or personal relationships that could have appeared to influence the work reported in this paper.

Acknowledgments

This work was supported by the Slovenian Research and Innovation Agency as core research program funding P1-0208, P2-0089, P1-0060, P1-0134, P1-0175, P2-0223 and project funding: J3-3079, J2-3043, J2-60047, J7-4420, and bilateral ARIS projects: BI-FR/23-24-PROTEUS-005 (PR-12039) and BI-RS/23-25-030 (PR-12782), Ministry of Education, Science and Sport and the European Regional Development Fund OP20.05187 RI-SI-EATRIS. The authors acknowledge the Centre of Excellence for Integrated Approaches in Chemistry and Biology of Proteins (CIPKeBiP) for providing access to facilities for the synthesis of the PMMA–siloxane–silica coating in a laboratory reactor. The authors also acknowledge the support of the Centre for Research Infrastructure at the University of Ljubljana, Faculty of Chemistry and Chemical Technology, which is part of the Network of Research and Infrastructural Centres UL (MRIC UL) and is financially supported by the Slovenian Research and Innovation Agency (ARIS; Infrastructure programme No. I0-0022) for the use of the Supernova diffractometer.

Appendix A. Supplementary data

Supplementary data to this article can be found online at https://doi.org/10.1016/j.ica.2025.122904.

Data availability

Data will be made available on request.

References

[1] C.D.S. Brites, S. Balabhadra, L.D. Carlos, Lanthanide-based thermometers: at the cutting-edge of luminescence thermometry, Adv. Opt. Mater. 7 (2019) 1801239, https://doi.org/10.1002/adom.201801239.

[2] C.D.S. Brites, R. Marin, M. Suta, A.N. Carneiro Neto, E. Ximendes, D. Jaque, L. D. Carlos, Spotlight on luminescence thermometry: basics, challenges, and cutting-edge applications, Adv. Mater. 35 (2023) 2302749, https://doi.org/10.1002/adma.202302749.

[3] I. Sedmak, I. Urbančič, J. Štrancar, M. Mortier, I. Golobič, Transient submicron temperature imaging based on the fluorescence emission in an Er/Yb co-doped glass–ceramic, Sens. Actuators A Phys. 230 (2015) 102–110, https://doi.org/10.1016/j.sna.2015.05.001.

[4] J. Zhou, B. Del Rosal, D. Jaque, S. Uchiyama, D. Jin, Advances and challenges for fluorescence nanothermometry, Nat. Methods 17 (2020) 967–980, https://doi.org/10.1038/s41592-020-0957-y.

[5] H. Xiao, Q. Meng, C. Wang, Optical thermometry based on fluorescence intensity ratio of doped ions and matrix in CaWO4: Eu3+ phosphors, JOL 263 (2023) 119975, https://doi.org/10.1016/j.jlumin.2023.119975.

[6] X. Zhou, L. Chen, Z. Feng, S. Jiang, J. Lin, Y. Pang, L. Li, G. Xiang, Color tunable emission and low-temperature luminescent sensing of europium and terbium carboxylic acid complexes, Inorg. Chim. Acta 469 (2018) 576–582, https://doi.org/10.1016/j.ica.2017.10.014.

[7] Y. Zheng, Y. Meana, M.M.A. Mazza, J.D. Baker, P.J. Minnett, F.M. Raymo, Fluorescence switching for temperature sensing in water, J. Am. Chem. Soc. 144 (2022) 4759–4763, https://doi.org/10.1021/jacs.2c00820.

[8] J.S. Donner, S.A. Thompson, M.P. Kreuzer, G. Baffou, R. Quidant, Mapping intracellular temperature using green fluorescent protein, Nano Lett. 12 (2012) 2107–2111, https://doi.org/10.1021/nl300389y.

[9] J. Qiao, L. Qi, Y. Shen, L. Zhao, C. Qi, D. Shangguan, L. Mao, Y. Chen, Thermal responsive fluorescent block copolymer for intracellular temperature sensing, J. Mater. Chem. 22 (2012) 11543, https://doi.org/10.1039/c2jm31093g.

[10] R.M. Diaz-Rodriguez, D.A. Gálico, D. Chartrand, E.A. Suturina, M. Murugesu, Toward opto-structural correlation to investigate luminescence thermometry in an organometallic Eu(II) complex, J. Am. Chem. Soc. 144 (2022) 912–921, https://doi.org/10.1021/jacs.1c11076.

[11] J. Liu, L. Lu, X. Liu, X. Mi, Study on the photoluminescence performance and thermal sensitivity of (Y,Gd)2O3:Tb3+,Dy3+,Tm3+ phosphors, JOL 275 (2024) 120793, https://doi.org/10.1016/j.jlumin.2024.120793.

[12] Z.-T. Li, Z.-Q. Wang, Q.-Y. Liu, Y.-L. Wang, Three-dimensional lanthanide frameworks constructed of two-dimensional squares strung on one-dimensional double chains: syntheses, structures, and luminescent properties, Inorg. Chim. Acta 484 (2019) 13–18, https://doi.org/10.1016/j.ica.2018.09.017.

[13] C. Lewis, J.W. Erikson, D.A. Sanchez, C.E. McClure, G.P. Nordin, T.R. Munro, J. S. Colton, Use of machine learning with temporal photoluminescence signals from CdTe quantum dots for temperature measurement in microfluidic devices, ACS Appl. Nano Mater. 3 (2020) 4045–4053, https://doi.org/10.1021/acsanm.0c00065.

[14] Y. Wu, M.N.A. Alam, P. Balasubramanian, A. Ermakova, S. Fischer, H. Barth, M. Wagner, M. Raabe, F. Jelezko, T. Weil, Nanodiamond theranostic for light-controlled intracellular heating and nanoscale temperature sensing, Nano Lett. 21 (2021) 3780–3788, https://doi.org/10.1021/acs.nanolett.1c00043.

[15] L. Armelao, S. Quici, F. Barigelletti, G. Accorsi, G. Bottaro, M. Cavazzini, E. Tondello, Design of luminescent lanthanide complexes: from molecules to highly efficient photo-emitting materials, Coord. Chem. Rev. 254 (2010) 487–505, https://doi.org/10.1016/j.ccr.2009.07.025.

[16] Y. Dong, G. Li, L. Li, Europium(III) ion-based photoluminescence complexes of indole-derivative β-diketone dominated by ancillary ligands, Inorg. Chim. Acta 556 (2023) 121616, https://doi.org/10.1016/j.ica.2023.121616.

[17] X. Di, D. Wang, Q.P. Su, Y. Liu, J. Liao, M. Maddahfar, J. Zhou, D. Jin, Spatiotemporally mapping temperature dynamics of lysosomes and mitochondria using cascade organelle-targeting upconversion nanoparticles, Proc. Natl. Acad. Sci. U. S. A. 119 (2022) e2207402119, https://doi.org/10.1073/pnas.2207402119.

[18] A. Carlotto, L. Babetto, S. Carlotto, M. Miozzi, R. Seraglia, M. Casarin, G. Bottaro, M. Rancan, L. Armelao, Luminescent thermometers: from a library of europium(III) β-diketonates to a general model for predicting the thermometric behaviour of europium-based coordination systems, ChemPhotoChem 4 (2020) 674–684, https://doi.org/10.1002/cptc.202000116.

[19] Y. Song, L. Sun, J. Liu, Effect of rare earth ion on fluorescent properties of Eu(TTA) 3phen/PMMA temperature sensitive paint, Inorg. Chim. Acta 543 (2022) 121164, https://doi.org/10.1016/j.ica.2022.121164.

[20] A. Gonçalves, M.M. Da Cruz, L.O. Biscoli, N.A. Cabeza, J.T. Facco, H.L.B.V. De Barros, E.R. Botero, J.H. De Araujo-Neto, J. Ellena, A.R. Fiorucci, L.C.S. De Oliveira, J.M. Stropa, G.A. Casagrande, L.R.V. Favarin, D.C.M. Rodrigues, A. Dos Anjos, X-ray structure, chelation enhanced fluorescence effect, thermal and redox properties of a new europium(III) complex based on bioactive naphthoquinone, Inorg. Chim. Acta 558 (2023) 121758, https://doi.org/10.1016/j.ica.2023.121758.

[21] U. Cho, J.K. Chen, Lanthanide-based optical probes of biological systems, Cell Chem. Biol. 27 (2020) 921–936, https://doi.org/10.1016/j.chembiol.2020.07.009.

[22] J.-C.G. Bünzli, Lanthanide luminescence for biomedical analyses and imaging, Chem. Rev. 110 (2010) 2729–2755, https://doi.org/10.1021/cr900362e.

[23] J. Jia, P. Ren, H. Hu, N. Sayyadi, F. Parvin, X. Zheng, B. Shi, J.A. Piper, B. Song, K. Vickery, Y. Lu, Lifetime multiplexing with lanthanide complexes for luminescence *in situ* hybridisation, Anal. Sens. 2 (2022) e202100057, https://doi.org/10.1002/anse.202100057.

[24] Z. Zhu, B. Song, J. Yuan, C. Yang, Enabling the triplet of tetraphenylethene to sensitize the excited state of europium(III) for protein detection and time-resolved luminescence imaging, Adv. Sci. 3 (2016) 1600146, https://doi.org/10.1002/advs.201600146.

[25] D. Hamulić, P. Rodič, I. Milošev, The influence of length of alkyl chain on the chemical structure and corrosion resistance of silica-polyacrylic hybrid coatings on structural steel, Prog. Org. Coat. 150 (2021) 105982, https://doi.org/10.1016/j.porgcoat.2020.105982.

[26] P. Rodič, M. Lekka, F. Andreatta, L. Fedrizzi, I. Milošev, The effect of copolymerisation on the performance of acrylate-based hybrid sol-gel coating for corrosion protection of AA2024-T3, Prog. Org. Coat. 147 (2020) 105701, https://doi.org/10.1016/j.porgcoat.2020.105701.

[27] D. Hamulić, G. Medoš, D. Korte, P. Rodič, I. Milošev, The effect of curing temperature and thickness of polybutyl methacrylate siloxane coatings on the corrosion protection of structural steel S355, Coatings 13 (2023) 675, https://doi.org/10.3390/coatings13040675.

[28] I. Milošev, D. Hamulić, P. Rodič, C. Carrière, S. Zanna, H. Budasheva, D. Korte, M. Franko, D. Mercier, A. Seyeux, P. Marcus, Siloxane polyacrylic sol-gel coatings with alkly and perfluoroalkyl chains: synthesis, composition, thermal properties and log-term corrosion protection, Appl. Surf. Sci. 574 (2022) 151578, https://doi.org/10.1016/j.apsusc.2021.151578.

[29] P. Rodič, R.C. Korošec, B. Kapun, A. Mertelj, I. Milošev, Acrylate-based hybrid sol-gel coating for corrosion protection of AA7075-T6 in aircraft applications: the effect of copolymerization time, Polymers 12 (2020) 948, https://doi.org/10.3390/polym12040948.

[30] I. Sedmak, I. Urbančič, R. Podlipec, J. Štrancar, M. Mortier, I. Golobič, Submicron thermal imaging of a nucleate boiling process using fluorescence microscopy, Energy 109 (2016) 436–445, https://doi.org/10.1016/j.energy.2016.04.121.

[31] I. Sedmak, R. Podlipec, I. Urbančič, J. Štrancar, M. Mortier, I. Golobič, Spatially resolved temperature distribution in a rare-earth-doped transparent glass-ceramic, Sensors 22 (2022) 1970, https://doi.org/10.3390/s22051970.
[32] Y. Liu, G. Liu, W. Zhou, G. Feng, Q. Ma, Y. Zhang, G. Xing, In situ self-assembled J-aggregate nanofibers of glycosylated Aza-BODIPY for synergetic cell membrane disruption and type I photodynamic therapy, Angew. Chem. Int. Ed. 62 (2023) e202309786, https://doi.org/10.1002/anie.202309786.
[33] J.G. Croissant, C. Mauriello-Jimenez, M. Maynadier, X. Cattoën, M. Wong Chi Man, L. Raehm, O. Mongin, M. Blanchard-Desce, M. Garcia, M. Gary-Bobo, P. Maillard, J.-O. Durand, Synthesis of disulfide-based biodegradable bridged silsesquioxane nanoparticles for two-photon imaging and therapy of cancer cells, Chem. Commun. 51 (2015) 12324–12327, https://doi.org/10.1039/C5CC03736K.
[34] O.V. Dolomanov, L.J. Bourhis, R.J. Gildea, J.A.K. Howard, H. Puschmann, OLEX2: a complete structure solution, refinement and analysis program, J. Appl. Cryst. 42 (2009) 339–341, https://doi.org/10.1107/S0021889808042726.
[35] C.F. Macrae, P.R. Edgington, P. McCabe, E. Pidcock, G.P. Shields, R. Taylor, M. Towler, J. van de Streek, Mercury: visualization and analysis of crystal structures, J. Appl. Cryst. 39 (2006) 453–457, https://doi.org/10.1107/S002188980600731X.
[36] E. Girotto, A. Pereira, C. Arantes, M. Cremona, A.J. Bortoluzzi, C.A.M. Salla, I. H. Bechtold, H. Gallardo, Efficient terbium complex based on a novel pyrazolone derivative ligand used in solution-processed OLEDs, JOL 208 (2019) 57–62, https://doi.org/10.1016/j.jlumin.2018.12.027.
[37] V.K. Sthalam, A.K. Singh, S. Pabbaraja, An integrated continuous flow micro-total ultrafast process system (μ-TUFPS) for the synthesis of celecoxib and other cyclooxygenase inhibitors, Org. Process Res. Dev. 23 (2019) 1892–1899, https://doi.org/10.1021/acs.oprd.9b00212.
[38] H.A. Flaxman, D.K. Miyamoto, C.M. Woo, Small molecule interactome mapping by photo-affinity Labeling (SIM-PAL) to identify binding sites of small molecules on a proteome-wide scale, Curr. Protoc. Chem. Biol. 11 (2019) e75, https://doi.org/10.1002/cpch.75.
[39] W. Holzer, S. Bieringer, 4-Acyl-5-hydroxy-1-phenyl-3-trifluoromethylpyrazoles: synthesis and NMR spectral investigations, Heterocycles 68 (2006) 1825, https://doi.org/10.3987/COM-05-10502.
[40] Y. Zhang, H. Shi, Y. Ke, Y. Cao, Synthesis and characterization of highly fluorescent europium functionalized β-diketonate complexes, JOL 124 (2007) 51–57, https://doi.org/10.1016/j.jlumin.2006.01.361.
[41] K. Nehra, A. Dalal, A. Hooda, S. Singh, D. Singh, S. Kumar, Spectroscopic and optical investigation of 1,10-phenanthroline based Tb(III) β-diketonate complexes, Inorg. Chim. Acta 536 (2022) 120860, https://doi.org/10.1016/j.ica.2022.120860.
[42] S. Dasari, S. Singh, S. Sivakumar, A.K. Patra, Dual-sensitized luminescent europium (III) and terbium(III) complexes as bioimaging and light-responsive therapeutic agents, Chem. Eur. J. 22 (2016) 17387–17396, https://doi.org/10.1002/chem.201603453.
[43] A. Dalal, K. Nehra, A. Hooda, D. Singh, K. Jakhar, S. Kumar, Preparation and photoluminescent characteristics of green Tb(III) complexes with β-diketones and N donor auxiliary ligands, Inorg. Chem. Commun. 139 (2022) 109349, https://doi.org/10.1016/j.inoche.2022.109349.
[44] P. Rodič, B. Kapun, I. Milošev, Durable polyacrylic/siloxane-silica coating for the protection of cast AlSi7Mg0.3 alloy against corrosion in chloride solution, Polymers 15 (2023) 3993, https://doi.org/10.3390/polym15193993.
[45] M. Manuela Silva, V. De Zea Bermudez, L.D. Carlos, A. Paula Passos De Almeida, M. J. Smith, Sol-gel processing and structural study of europium-doped hybrid materials, J. Mater. Chem. 9 (1999) 1735–1740, https://doi.org/10.1039/a901587f.
[46] M. Li, C. Wang, D. Wang, J. Li, Structure-dependent photoluminescence of europium(III) coordination oligomeric silsesquioxane: synthesis and mechanism, ACS Omega 6 (2021) 227–238, https://doi.org/10.1021/acsomega.0c04365.
[47] P. Rodič, S. Zanna, I. Milošev, P. Marcus, Degradation of sol-gel acrylic coatings based on Si and Zr investigated using electrochemical impedance, infrared and X-ray photoelectron spectroscopies, Front. Mater. 8 (2021) 756447, https://doi.org/10.3389/fmats.2021.756447.
[48] A.P. Duarte, L. Mauline, M. Gressier, J. Dexpert-Ghys, C. Roques, J.M.A. Caiut, E. Deffune, D.C.G. Maia, I.Z. Carlos, A.A.P. Ferreira, S.J.L. Ribeiro, M.-J. Menu, Organosilylated complex [Eu(TTA)$_3$ (Bpy-Si)]: a bifunctional moiety for the engineering of luminescent silica-based nanoparticles for bioimaging, Langmuir 29 (2013) 5878–5888, https://doi.org/10.1021/la400365c.